Nano-Micro Letters
e-ISSN 2150-5551
CN 31-2103/TB
ARTICLE
https://doi.org/10.1007/s40820-024-01371-y

Cite as
Nano-Micro Lett.
(2024) 16:143

Received: 5 December 2023
Accepted: 23 January 2024

Kinetic-Thermodynamic Promotion Engineering toward High-Density Hierarchical and Zn-Doping Activity-Enhancing ZnNiO@CF for High-Capacity Desalination

Jie Ma[1,2,3], Siyang Xing[2,3,5], Yabo Wang[2], Jinhu Yang[4], Fei Yu[1] ✉

HIGHLIGHTS

- Through facial basicity adjustment, kinetically favorable $Zn_xNi_{1-x}O$@CF electrode was formed with a high density hierarchical structure and three dimensional open pores.
- The optimal Zn-doping ratio in $Zn_xNi_{1-x}O$@CF has excellent sodium storage and desalination performance (128.9 mg g^{-1}).
- The mechanism of Na^+ intercalation process was studied by electrochemical quartz crystal microbalance with dissipation monitoring in situ test and the activation mechanism of redox-inert Zn-doping on electrode materials was reported.

ABSTRACT Despite the promising potential of transition metal oxides (TMOs) as capacitive deionization (CDI) electrodes, the actual capacity of TMOs electrodes for sodium storage is significantly lower than the theoretical capacity, posing a major obstacle. Herein, we prepared the kinetically favorable $Zn_xNi_{1-x}O$ electrode in situ growth on carbon felt ($Zn_xNi_{1-x}O$@CF) through constraining the rate of OH^- generation in the hydrothermal method. $Zn_xNi_{1-x}O$@CF exhibited a high-density hierarchical nanosheet structure with three-dimensional open pores, benefitting the ion transport/electron transfer. And tuning the moderate amount of redox-inert Zn-doping can enhance surface electroactive sites, actual activity of redox-active Ni species, and lower adsorption energy, promoting the adsorption kinetic and thermodynamic of the $Zn_{0.2}Ni_{0.8}O$@CF. Benefitting from the kinetic-thermodynamic facilitation mechanism, $Zn_{0.2}Ni_{0.8}O$@CF achieved ultrahigh desalination capacity (128.9 mg_{NaCl} g^{-1}), ultra-low energy consumption (0.164 kW h kg_{NaCl}^{-1}), high salt removal rate (1.21 mg_{NaCl} g^{-1} min^{-1}), and good cyclability. The thermodynamic facilitation and Na^+ intercalation mechanism of $Zn_{0.2}Ni_{0.8}O$@CF are identified by the density functional theory calculations and electrochemical quartz crystal microbalance with dissipation monitoring, respectively. This research provides new insights into controlling electrochemically favorable morphology and demonstrates that Zn-doping, which is redox-inert, is essential for enhancing the electrochemical performance of CDI electrodes.

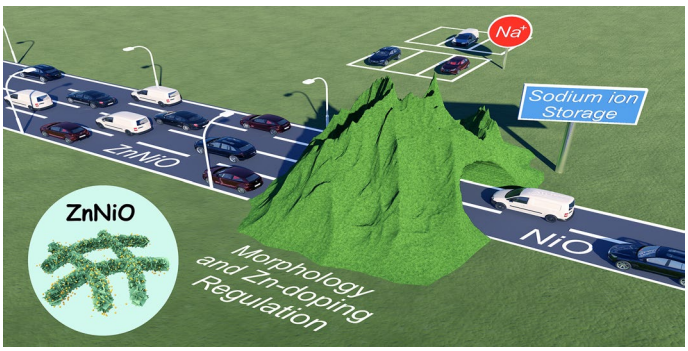

KEYWORDS Zinc–nickel metal oxide; High-density hierarchical; Capacitive deionization; Zinc-doping

✉ Fei Yu, fyu@vip.163.com
[1] College of Marine Ecology and Environment, Shanghai Ocean University, 201306 Shanghai, People's Republic of China
[2] School of Civil Engineering, Kashi University, 844000 Kashi, People's Republic of China
[3] Research Center for Environmental Functional Materials, College of Environmental Science and Engineering, Tongji University, 1239 Siping Road, 200092 Shanghai, People's Republic of China
[4] School of Chemical Science and Engineering, Tongji University, 1239 Siping Road, 200092 Shanghai, People's Republic of China
[5] Department of Energy, Environmental & Chemical Engineering, Washington University in St. Louis, St. Louis, MO 63130, USA

Published online: 04 March 2024

1 Introduction

Due to its ease of operation, reduced energy cost, and high work efficiency in comparison with traditional desalination technologies, the capacitive deionization (CDI) technology offers considerable potential to address the severe global water shortage problem [1]. Ion-capture mechanisms in CDI are generally similar to those in sodium-ion batteries (SIBs). Consequently, considerable effort has been devoted to exploring the potential of SIBs as cathode materials for CDI processes [2, 3]. Carbonaceous materials, via the electrical double layer (EDL) mechanism [4–6], had hit a roadblock due to their low adsorption capacity (usually < 25 mg g^{-1}) and potential for side reactions [7]. The non-carbon electrode materials mainly included transition metal oxides (TMOs) [8–13], Prussian blue analogs [14–16], polyanionic phosphates [17, 18], MXene [19–21], and layered double hydroxide (LDH) [22, 23], and can achieve high capacity desalination by redox reaction [24]. Among these materials, TMOs comprising the advantages of easy preparation, element diversity, facile morphology control, excellent reversible intercalation pseudocapacity and promising sodium storage theoretical capacitance, have shown great potential for application in CDI [11, 12, 25–33].

However, TMOs still suffers from issues with stacking and poor electrical conductivity, which limit their sodium ion intercalation capacity to a certain extent. In addition, the large size of sodium ions leads to the slow sodiation/desodiation reaction kinetics, resulting in a significantly lower capacity for sodium storage than theoretically possible [28, 29, 32–35]. For example, in the present study [26, 27, 36, 37], even the state-of-the-art electrodes of NiO can only reach about 75% of the theoretical capacity, 2573 F g^{-1} within 0.5 V [38], severely impeding their application [39]. Substantial efforts have been undertaken to enhance the reaction kinetics by the creation of various nanostructures to boost electron conduction and reduce the ion diffusion pathway, thereby reducing energy consumption and increasing adsorption rates [40, 41]. As well, it has been argued that by decreasing the electrode size to a certain nanoscale level, the battery-type electrode material will behave similarly to a capacitive electrode [42, 43]. which made it had battery-level storage capacity combined with both cycle life and adsorption rate. For instance, $NiCo_2O_4$@NiCo-LDH can form different nanostructures depending on the hydrothermal synthesis time, where the optimal nanostructure exhibits a capacitance of up to 5810 mF cm^{-2} [44]. It was also discovered that the ion conductivity of $Li_{10}GeP_2S_{12}$ increases as the particle volume decreases when using advanced nanoscale modeling techniques [45].

Despite the advances made, the actual capacity was still far from the theoretical one, even at an ultralow rate, suggesting that there may be thermodynamic difficulties in sodium storage in addition to the electrochemical kinetics limitations. It was possible to promote sodium intercalation both kinetically and thermodynamically by transition metal doping [46–48]. Transition-metal doping essentially reduced the sodium intercalation energies, rearranged electron distribution and enabled a complete adsorption reaction [39]. Among the promising and hot candidates for electrochemical energy storage and conversion, zinc (Zn) has been widely studied. The doping of Zn in electrode materials had been reported to typically exhibit specific characteristics such as increased electronic conductivity, reaction activity, and surface roughness, resulting in improved electrochemical properties [49–51]. The incorporation of Zn into the ZnNiCo-P can boost charge transfer and enhance ion adsorption processes, considerably improving the electrochemical performance [51]. However, over-doping of Zn may lead to the formation of by-products, as well as instability in the crystallization of the material, resulting in partial leaching/dissolution of the material [11, 49]. Based on the above consideration, it was highly promising for advanced CDI cathodes to find a simple method to adjust the microscopic morphology of electrodes and construct chemically stable electrodes with dual kinetic-thermodynamic enhancement by an appropriate amount of Zn-doping.

Herein, a redox-inert Zn-doping activated high-density hierarchical $Zn_{0.2}Ni_{0.8}O$@CF electrode was conveniently synthesized via a one-step hydrothermal method. Simple adjustment of the basicity of the hydrothermal conditions could constrain the rate of OH^- production and thus the number of lamellar nuclei formation, giving this electrode a kinetically favorable nanostructure, i.e., increased ion-accessible surface sites and a high-speed ion conduction network. $Zn_{0.2}Ni_{0.8}O$ electrode demonstrated exceptional CDI performance with outstanding desalination capacity of 128.9 mg_{NaCl} g^{-1}, excellent cycling stability and ultralow energy consumption, which exceeding the desalination capacity of other state-of-the-art CDI electrodes at similar conditions. The density functional theory (DFT) and ex situ

 https://doi.org/10.1007/s40820-024-01371-y

XPS analysis showed that Zn doping could not only enhance the electron transfer kinetics through improved conductivity but lower the Na^+ adsorption energy and improve the adsorption thermodynamics, through enhancing the real activity of surface electroactive sites and redox-active Ni species. Electrochemical quartz crystal microbalance with dissipation monitoring (EQCM-D) revealed the mechanism and high reversibility of Na^+ intercalation. This work provided a new perspective on a simple way to regulate electrochemically favorable nanomorphology and the critical role of redox-inert Zn-doping as an active promoter for advanced CDI electorate design.

2 Experimental

2.1 Materials Preparation

A piece of 3 cm × 3 cm × 0.1 cm carbon felt was immersed in a mixture of H_2SO_4 (98%) and HNO_3 (68%) at a volume ratio of 1:3 and placed in a water bath at 80 °C for 3 h. The carbon felt was then removed from the mixture and rinsed with deionized water to a neutral pH and get the prefabricated carbon felt.

To prepare $Zn_xNi_{1-x}(OH)_2$ carbon felt electrode, 6 g of urea, 3.7 g of NH_4F, 14.75 g of $Ni(NO_3)_2{\cdot}6H_2O$, and 1.48 g of $Zn(NO_3)_2{\cdot}6H_2O$ were dissolved in a volume of 500 mL of deionized water at room temperature in to obtain mixture A. The pH of the pre-solution was adjusted to 4. The hydration reactor contained pCF and pre-solution A was sealed at a constant temperature (140 °C) for 2 h to obtain a prefabricated carbon felt electrodes with surface loading of $Zn_xNi_{1-x}(OH)_2$. The dried $Zn_xNi_{1-x}(OH)_2$ was placed in a tube furnace with nitrogen gas environment to obtain a $Zn_xNi_{1-x}O$ electrode. More details are in Sect. S3 of Supporting Information.

2.2 Electrochemical Test

The $Zn_xNi_{1-x}O$ were directly used as working electrode. An electrochemical station (CHI660D, Chenhua Instruments Co.) was used for all electrochemical tests. CV was swept between − 0.4 and 0.8 V under certain scan rates (1–60 mV s^{-1}), and GCD was measured at the uniform voltage window with various specific currents (1–6 mA cm^{-2}). Cyclic voltammetry (CV), galvanostatic charging/discharging (GCD), and electrochemical impedance spectroscopy (EIS) tests were conducted on a three-electrode system consisting of a working electrode, Pt (counter electrode), and Ag/AgCl (reference electrode) in 1 M NaCl. More details are in Sect. S3 of Supporting Information.

2.3 Desalination Experiments

The flow-by CDI stack is composed of glass plates, silica gel gaskets, a cation/anion exchange membrane (CEM/AEM), and a chamber with dimensions of 0.8 cm × 4 cm × 4 cm. An activated carbon electrode served as the anode, and a $Zn_xNi_{1-x}O$ electrode served as the cathode. All desalination experiments were carried out under a constant current with a fixed flow rate, a fixed initial NaCl concentration and a fixed volume, while other operational parameters, including the different activated electrodes, current density, were varied to obtain the best desalination capacity. More details are in Section S4.

3 Results and Discussion

3.1 Material Characterization of $Zn_xNi_{1-x}O$@CF

Control the elemental ratio of Zn–Ni dosage of 1:4, a one-step hydrothermal method was used to synthesize $Zn_{0.2}Ni_{0.8}(OH)_2$ nanosheets in situ on the surface of prefabricated CF and we obtained $Zn_{0.2}Ni_{0.8}O$@CF electrodes by annealing at 500 °C (Fig. 1a). Samples obtained based on pre-mixtures of different basicity (pH = 2, 4, and 6), named $Zn_{0.2}Ni_{0.8}O$@CF-2, $Zn_{0.2}Ni_{0.8}O$@CF-4, and $Zn_{0.2}Ni_{0.8}O$@CF-6, respectively (more details in Supporting Information). Distinctive from routine methods, we found that alterations in the basicity of the hydrothermal conditions may have a considerable effect on electrode morphology (Fig. 1b–d). $Zn_{0.2}Ni_{0.8}O$@CF-4 nanosheets with diameter of about 500 ~ 1500 nm and thickness of 30 ~ 60 nm would be formed in situ on CF in a high-density hierarchical structure. The $Zn_{0.2}Ni_{0.8}O$@CF-4 had a loosely packed morphology, but the nanosheets were strongly connected, which increased electrolyte permeability and formed the improved electron pathways by the formation of three-dimensional networks. This resulted in a faster sodiation adsorption kinetics and an enhanced pseudocapacitance [52]. Base dissociation rates determined the reaction kinetics between the metal precursor

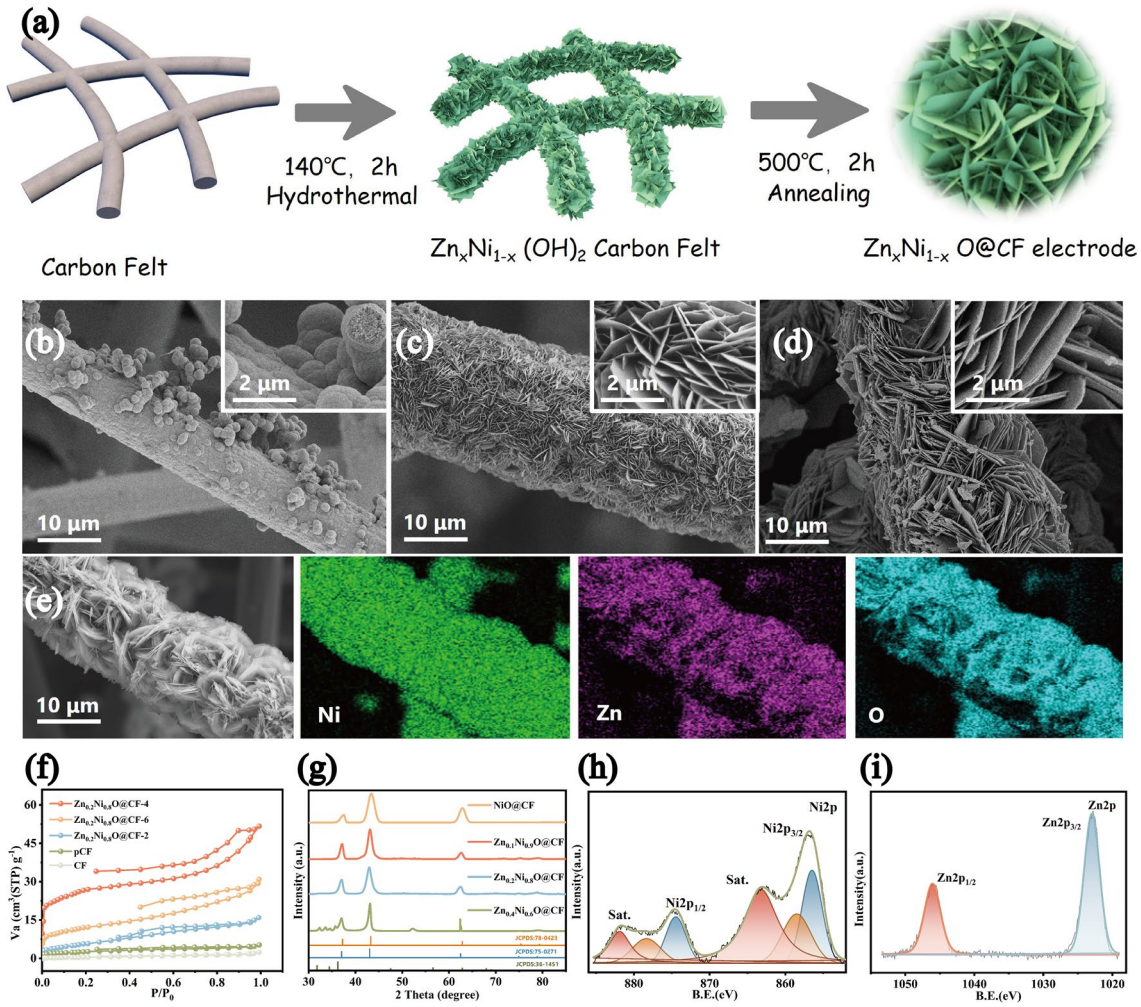

Fig. 1 **a** Schematic illustration of the layer $Zn_xNi_{1-x}O$@CF preparation. SEM of the **b** $Zn_{0.2}Ni_{0.8}O$@CF-2, **c** $Zn_{0.2}Ni_{0.8}O$@CF-4 and **d** $Zn_{0.2}Ni_{0.8}O$@CF-6. **e** EDS mapping image of $Zn_{0.2}Ni_{0.8}O$@CF-4, **f** N_2 adsorption/desorption isotherms and **g** XRD patterns of $Zn_xNi_{1-x}O$@CF with different Zn-doping. XPS spectrum of Ni 2*p* **h** and Zn 2*p* **i** for $Zn_{0.2}Ni_{0.8}O$@CF

counterions and dissociated OH^-, resulting in different morphologies [53]. However, when the pH of the pre-solution is 2, the surface of CF formed micron porous spheres without the formation of sheet structure; when the pH = 6, the sheets were larger and thicker, with more serious stacking phenomenon. On the basis of this assumption, by regulating the pH of the pre-solution to regulate basicity of hydrothermal condition, a high-density hierarchical layered $Zn_{0.2}Ni_{0.8}O$@CF would be produced in an energetically favorable state (Fig. 1c) and possess the best electrochemical properties, which could be explained by Ostwald ripening [54, 55]. As shown in Fig. 1e, the results of energy dispersive spectrometer (EDS) mapping showed that Zn, Ni, and O elements were evenly spread across the surface of carbon felts, demonstrating the successful synthesis of $Zn_{0.2}Ni_{0.8}O$@CF; in addition, C cannot be observed almost in the region where the nanosheets were attached, also indicating the synthesis of a high-density $Zn_{0.2}Ni_{0.8}O$@CF layer structure on the carbon fiber surface.

Figures 1f and S1 display the specific surface area (SSA) and corresponding pore size distribution (PSD) results. $Zn_{0.2}Ni_{0.8}O$@CF-4 exhibited a type IV isotherm and had the largest SSA (94.341 $m^2\ g^{-1}$, Table S1), which was the signature of hierarchical micro-mesoporous structure and consistent with the BJH pore size fitting results. Microporous structure could enhance the desalination capacity by

 https://doi.org/10.1007/s40820-024-01371-y

offering multiple adsorption sites for ion accommodation; while the mesopores facilitated ion transport due to their wide pore openings and thus enhanced the desalination rate [56, 57]. In contrast, other simples exhibited the type III N_2-sorption isotherm indicating there were no pores or a little microporous. This was because, under more reasonable hydrothermal conditions, the $Zn_{0.2}Ni_{0.8}O$@CF sheet structure was more homogeneous and less self-stacking (compared to Fig. 1d), which eventually formed a rich pore structure and fast ion transport pathways. In this case, the pre-solution preparation condition of pH = 4 was chosen in all later experiments. Therefore, the material was named as $Zn_{0.2}Ni_{0.8}O$@CF.

The XRD of prepared $Zn_{0.2}Ni_{0.8}O$@CF in different pH conditions (Fig. S2) all matched well with the $Zn_{0.2}Ni_{0.8}O$@CF standard spectrum (JCPDS No. 75-0271), and combined with the absence of peaks of ZnO and the presence of Zn element in the electrode (Fig. 1e), suggested that Zn was doped in the $Zn_{0.2}Ni_{0.8}O$@CF crystalline phase rather than just physically blending two unary phases. The higher peak strength of the $Zn_{0.2}Ni_{0.8}O$@CF materials was also attributed to the Zn-doping, indicating a higher degree of crystallinity. However, this conclusion did not apply in all cases. We also adjusted the dosing ratios of Zn and Ni and named them as NiO@CF, $Zn_{0.1}Ni_{0.9}O$@CF and $Zn_{0.4}Ni_{0.6}O$@CF, respectively. As shown in Fig. 1g, when Zn was added in a certain range, Zn was mainly doped in the crystalline phase of NiO: $Zn_{0.1}Ni_{0.9}O$@CF and $Zn_{0.2}Ni_{0.8}O$@CF exhibited XRD patterns similar to NiO (JCPDS No. 78-0423); but when the proportion of Zn-doping increased (such as $Zn_{0.4}Ni_{0.6}O$@CF), the crystalline phase of ZnO appears (JCPDS No. 36-1451), destabilizing the crystal and making it easier to decompose [11], resulting in less electrochemical stability for the electrodes. Jia et al. [46] also found that the ratio of Zn-doping was essential for improving the electrochemical performance. Therefore, to further investigate the effect of Zn-doping amount, different Zn-doping ratios on the electrode performance were mainly discussed in the subsequent investigations.

The chemical states of different $Zn_xNi_{1-x}O$@CF simples were investigated via XPS (Fig. S3a). Two spin–orbit splitting peaks with a spin-energy separation of 17.6 eV were observed in the high-resolution spectra of Ni 2*p* (Fig. 1h) [58–60]. The Zn 2*p* spectra in Fig. 1i showed the Zn $2p_{1/2}$ and Zn $2p_{3/2}$ peaks of the Zn 2*p* doublet at approximately 1045.87 and 1022.89 eV, respectively [61]. It also provided the exact formulas of $Zn_xNi_{1-x}O$, which was $Zn_{0.12}Ni_{0.88}O$, $Zn_{0.18}Ni_{0.82}O$, and $Zn_{0.31}Ni_{0.69}O$ and closed to the theoretical ratio. O 1*s* (Fig. S3b) could be decomposed into hydroxyl groups at the surface, O^{2-} ions in the crystal structure, and carbon dioxide or adsorbed water molecules. The presence of interfacial OH^- contributed to the hydrophilicity of $Zn_xNi_{1-x}O$@CF, which was confirmed by the ultralow water contact angle (Fig. S4). Additionally, the hydration shells or crystallographic water formed in metal oxides could speed up the ion transport [62].

3.2 Electrochemical Properties

Electrochemical tests were performed in a 1 mol L^{-1} NaCl solution using a three-electrode system to further investigate the $Zn_xNi_{1-x}O$@CF electrode performance and the effect of different Zn-doping amounts. CV curves of the electrodes presented a quasi-rectangular shape without prominent redox peaks (Fig. 2a), indicating that the sodium storage mechanism could be attributed to pseudocapacitance [63]. Regardless of the sweep speeds tested, $Zn_{0.2}Ni_{0.8}O$@CF consistently exhibited the highest area-specific capacity among the four materials (Figs. 2b and S5a) and the best electrochemical performance (414.647 mF cm^{-2} at 1 mV s^{-1}), and its capacity reached 247.09 mF cm^{-2} at 20 mV s^{-1}, 1.25 times that of $Zn_{0.1}Ni_{0.9}O$@CF and 1.59 times that of NiO@CF. Considering the redox-inert effect of the Zn in the pseudocapacitance storage [46, 51], the specific capacity of $Zn_{0.2}Ni_{0.8}O$@CF electrode (18% redox-inert Zn/82% redox-active Ni) was even slightly superior to the NiO@CF electrode (100% redox-active Ni), indicating Zn-doping of the $Zn_{0.2}Ni_{0.8}O$@CF material could promote activity through underlying mechanisms. The poor performance of $Zn_{0.4}Ni_{0.6}O$@CF electrode may be attributed to the ZnO phase formation due to the redundant zinc salt (Fig. 1i), resulting in a blend of ZnO and $Zn_xNi_{1-x}O$.

Therefore, the Zn: Ni ratio of the pre-mixture solution was set to 1:4. The CV curves in Fig. 2c showed similar trends at different scan rates exhibited excellent capacitive reversibility of $Zn_{0.2}Ni_{0.8}O$@CF, which was also characterized by repeated CV cycling and displayed no significant change after 100 cycles at 10 mV s^{-1} (Fig. 2d). The

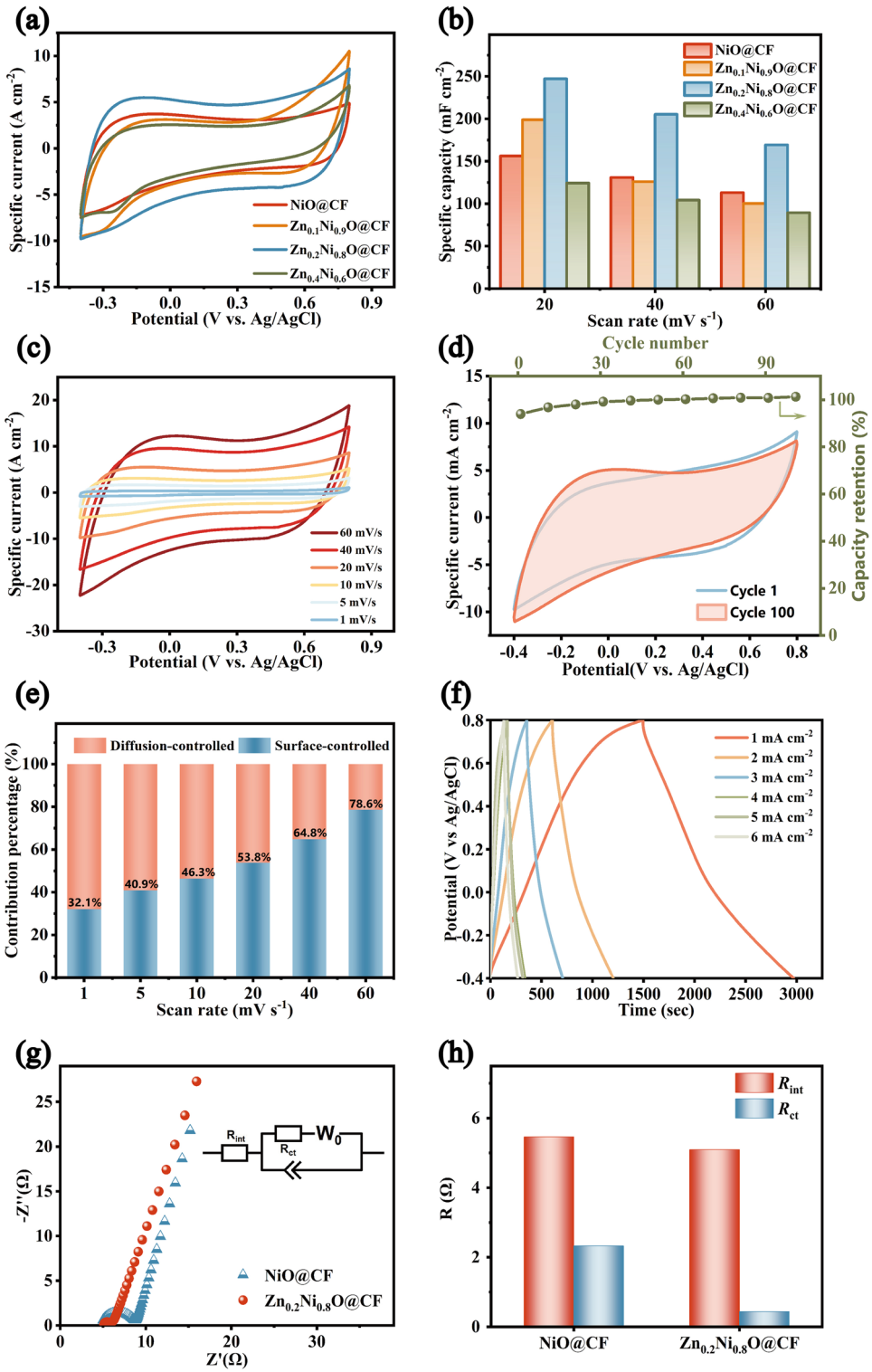

Fig. 2 **a** CV curves of NiO@CF, $Zn_{0.1}Ni_{0.9}O$@CF, $Zn_{0.2}Ni_{0.8}O$@CF and $Zn_{0.4}Ni_{0.6}O$@CF and **b** specific capacity of various scan rates. **c** CV curves of $Zn_{0.2}Ni_{0.8}O$@CF measured at different scan rates and **d** after 100 cycles at 10 mV s^{-1}. **e** Normalized contribution ratios of surface-/diffusion-controlled capacities and **f** GCD profiles of $Zn_{0.2}Ni_{0.8}O$@CF. **g** Nyquist plots and **h** simulated internal and charge transfer resistance of NiO@CF and $Zn_{0.2}Ni_{0.8}O$@CF

https://doi.org/10.1007/s40820-024-01371-y

high-level capacity retention was also related to the high homogeneity of the hierarchical interconnected nanosheet network, effectively mitigating the bulk phase expansion of ion intercalation [64, 65].

In addition, Fig. 2e explores the current contribution of the surface- and diffusion-control process of the $Zn_{0.2}Ni_{0.8}O$@CF electrode. As shown in Figs. 2e and S5b, c, the $Zn_{0.2}Ni_{0.8}O$@CF electrode showed a dominant capacitive contribution, reaching a maximum of 78.6% at 60 mV s^{-1}. It has been suggested that battery-like electrode materials can exhibit capacitive behavior when their size is reduced to a certain nanoscale level (typically less than 10 nm) [43], which may explain the high pseudocapacitance of the $Zn_{0.2}Ni_{0.8}O$@CF electrode, likely due to the kinetic promotion of the redox reaction on the surface of the ultrathin nanosheets. Besides, no plateau occurred in galvanostatic charge–discharge (GCD) profiles (Fig. 2f), which further demonstrated the pseudocapacitance behavior and indicated that adsorption reactions were occurring at the surface rather than in the bulk. These may be attributed to the low degree of stacking of the nanosheets obtained by morphological modulation with a highly open structure and short diffusion pathways, which enabled the electrodes to possess a high number of active sites and faster reaction kinetics [52, 66, 67]. Above all, the Na^+ removal process was shown by Eqs. (1) and (2):

$$Zn_{0.2}Ni_{0.8}O + xNa^+ + xe^- \rightarrow Na_xZn_{0.2}Ni_{0.8}O \quad (1)$$

$$Zn_{0.2}Ni_{0.8}O(OH)_n^- + nNa^+ \rightarrow Zn_{0.2}Ni_{0.8}O(OH)_nNa_x \quad (2)$$

To further investigate the effectiveness of Zn-doping, electrochemical impedance measurements (EIS) were measured (Fig. 2g). Parameters fitted values were shown in Fig. 2h and Table S2. $Zn_{0.2}Ni_{0.8}O$@CF electrode showed lower internal resistance (R_{int}) value (5.10 Ω) compared to NiO@CF (5.46 Ω), indicating a lower proportion of internal resistance to charge consumption and higher charge efficiency. The charge transfer resistance (R_{ct}) value of the $Zn_{0.2}Ni_{0.8}O$@CF electrode (0.44 Ω) was also lower than NiO@CF (2.33 Ω), which meant $Zn_{0.2}Ni_{0.8}O$@CF had a better conductivity and superior electrochemical kinetics [17].

3.3 CDI Performance

Activated carbon (AC) and the prepared materials were used as the cathode and the anode in CDI system with 1 g L^{-1} of NaCl, respectively (Fig. 3a). In constant current operation mode, specific current was a critical ingredient for engineering applications, as it was closely linked to energy consumption and desalination efficiency. At the specific current of 600 mA m^{-2}, specific adsorption capacity (SAC) of the $Zn_{0.2}Ni_{0.8}O$@CF electrode was as high as 128.9 ± 1.9 mg g^{-1}, which was the highest among all materials. $Zn_{0.2}Ni_{0.8}O$@CF electrode (18% redox-inert Zn/82% redox-active Ni) had a slightly higher SAC than the NiO electrode (100% redox-active Ni), also revealing the underlying activity-promoting mechanisms of Zn-doping.

As the current density returned to original level, the retention rate of $Zn_{0.2}Ni_{0.8}O$@CF electrode of SAC was 93.06% from Fig. 3b, and superior to the NiO electrode (86.91%), indicating that with appropriate Zn-doping, the crystal structure of $Zn_{0.2}Ni_{0.8}O$@CF remained relatively intact, and it had a high reversible capacity, which was also consistent with the analysis of $Zn_{0.2}Ni_{0.8}O$@CF crystallinity in XRD. SAC arising from current collector CF was negligible, thus the main capacity contribution came from $Zn_{0.2}Ni_{0.8}O$ material. Besides, a higher specific current led to a faster charge transfer (Fig. 3c), with a greater rate of electron transfer observed per unit time, resulting in a higher salt adsorption rate (SAR) [15, 68]. SAR was 6.81 ± 0.19 mg g^{-1} min^{-1} at 3000 mA m^{-2}, nearly six times greater than the rate at 600 mA m^{-2} (Fig. S6a) and practically one of the highest SAR materials available today (Table S3). The cut-off voltage, which marked the point of potential reversal, has a significant impact on the NaCl removal capacity. When the voltage interval expanded from −0.6/+0.6 to −1.4/+1.4 V, the desalination capacity of $Zn_{0.2}Ni_{0.8}O$@CF increased from 39.44 ± 0.18 to 198.3 ± 1.9 mg g^{-1} (Fig. 3d). Wider voltage intervals correspond to longer charging times. Consequently, a greater amount of charge was stored at the electrode, allowing it to take part in the desalination process. As shown in the CDI Ragone plot (Fig. 3e) of all prepared electrodes, it was clearly observed that the $Zn_{0.2}Ni_{0.8}O$@CF displays the highest SAR, SAC and better desalination performance. In addition, a comparison with samples synthesized at different pH conditions with different doping amounts was shown in Fig. S6b and also indicated that $Zn_{0.2}Ni_{0.8}O$@CF had the best desalination performance among all samples ($Zn_{0.4}Ni_{0.6}O$@CF had severe leaching due to crystal instability and the presence of ZnO [49], and the conductivity continued to rise, so the desalination capacity was not calculated). These results convincingly verified the excellent

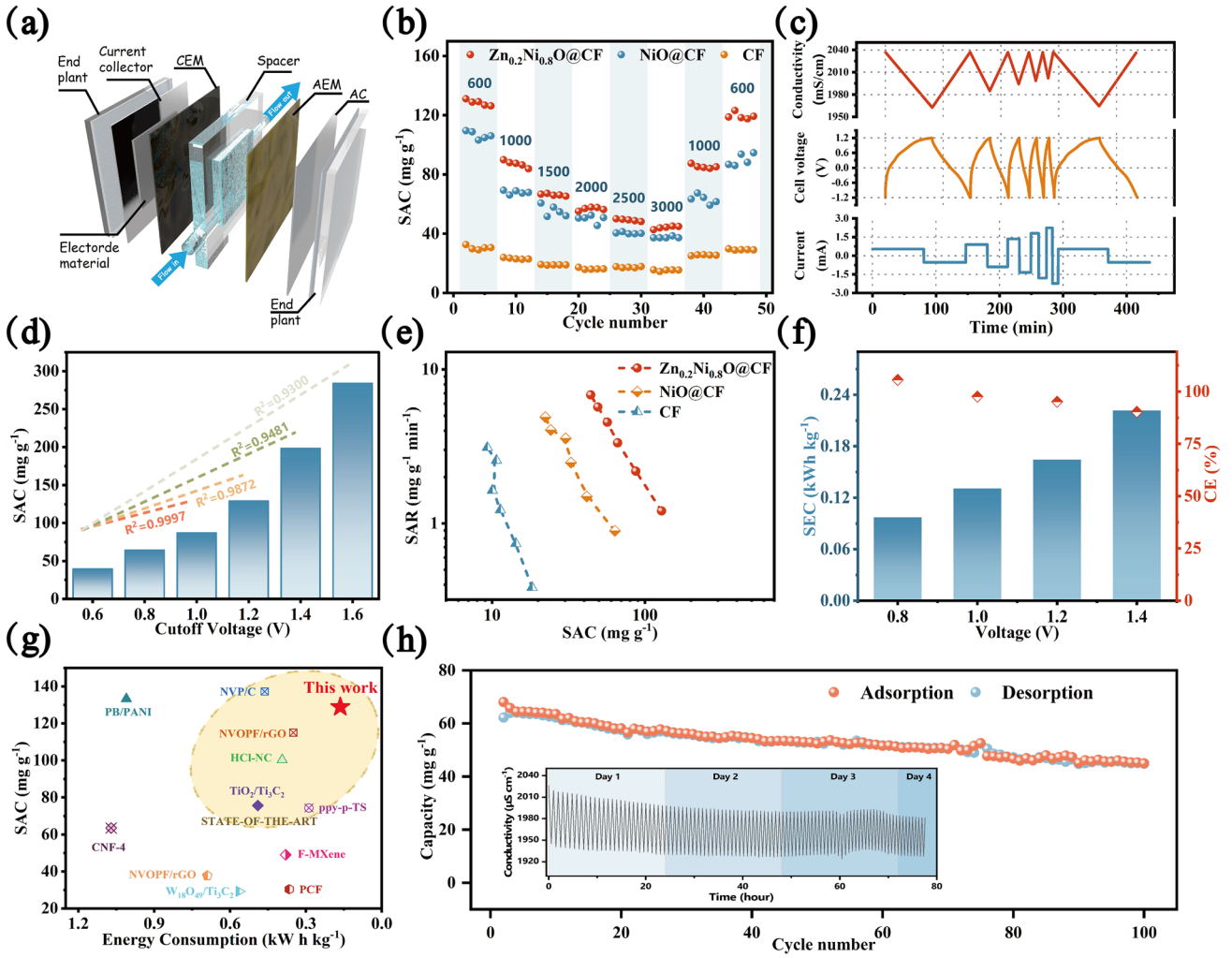

Fig. 3 **a** Schematic diagram of CDI process. **b** SAC of $Zn_{0.2}Ni_{0.8}O$, NiO and CF electrodes at different current densities. **c** The profiles of the conductivity, voltage, and current at various specific current. **d** SAC of $Zn_{0.2}Ni_{0.8}O$ at different cut-off voltages. **e** Ragone plots of various electrodes. **f** CE and SEC of $Zn_{0.2}Ni_{0.8}O$. **g** Comparison of SAC and SEC between $Zn_{0.2}Ni_{0.8}O$ and other state-of-the-art materials. **h** Cycling and regeneration performance of $Zn_{0.2}Ni_{0.8}O$ at 1500 mA m^{-2} over 100 cycles. Inset is the real-time conductivity and voltage profiles

desalination performance of the $Zn_{0.2}Ni_{0.8}O$@CF electrode and the underlying electrochemical enhancement mechanism of the Zn-doping.

A crucial metric for CDI performance was energy consumption [2]. When the voltage range was ± 1.2 V, the SEC of $Zn_{0.2}Ni_{0.8}O$@CF was 0.164 kW h kg^{-1} of NaCl, as shown in Fig. 3f, which increased to 0.222 kW h kg^{-1} of NaCl when the voltage interval was extended to ± 1.6 V, approaching the lower limit of constant-current CDI devices when tested in similar conditions [15, 56, 69]. The higher coulombic efficiency (CE) was close to 100% at all cut-off voltages, also leading to lower SEC. Accordingly, the energy recovery ratio was maintained at a stable value (28.6% ~ 23.6%) and was among the highest of the current cutting-edge electrodes (the recyclable energy was donated as E_a and E_c in Fig. S7), deriving from a lower ion diffusion energy barrier and promoted kinetics reaction [70] due to appropriate morphology control and Zn-doping. Unlike the commonly used Ragone diagram (known as Kin–Yoon diagram, SAR vs. SAC), we underlined the significance of energy consumption. SEC was a crucial metric in engineering practice due to the global energy crisis and the economic benefits of desalination. Compared with recently reported CDI electrodes (including carbonaceous and faradaic materials) (Fig. 3g) [15, 17, 18, 56, 70–77], it was clearly observed that $Zn_{0.2}Ni_{0.8}O$@CF displayed the highest SAC and lowest SEC among the

 https://doi.org/10.1007/s40820-024-01371-y

cutting-edge CDI electrodes. The excellent CDI performance of $Zn_{0.2}Ni_{0.8}O$@CF originated from kinetic promotion through a hierarchical nanosheet interconnection network structure with high active sites, enhanced intrinsic electron transfer and adsorbed activation of Zn-doping. Therefore, $Zn_{0.2}Ni_{0.8}O$@CF has the potential to be put into actual practice.

To further verify the long-term cycling performance of $Zn_{0.2}Ni_{0.8}O$@CF electrodes, 100 desalination cycles were carried out for about four days. The SAC of $Zn_{0.2}Ni_{0.8}O$@CF showed excellent reversibility of 86.2% (Fig. 3h), proving no signs of significant performance decay. Furthermore, the adsorption and desorption capacity remained nearly constant, indicating that the system was in a state of dynamic equilibrium (inset of Fig. 3h). Moreover, the morphology of $Zn_{0.2}Ni_{0.8}O$@CF nanosheets remained largely unchanged, except for slight aggregation, after 100 cycles (Fig. S8). In comparison to other carbon–metal composite electrodes, $Zn_{0.2}Ni_{0.8}O$@CF showed both a high capacity and excellent stability. The outstanding long-term performance demonstrated that $Zn_{0.2}Ni_{0.8}O$@CF would be a promising electrode for CDI application.

3.4 Desalination Mechanism

To further investigate the ion removal and charge storage kinetics, through the CV curves, we illustrated the power-law relationship. The current followed the law of diffusion-controlled if the *b*-value is about 0.5, which is usually seen in battery-like systems, while a value of 1.0 indicated an ideal surface-controlled case [23]. According to Fig. 4a, the calculated *b*-values were higher than 0.8 for all voltages. Such a high *b*-value was consistent with strong pseudocapacitive nature of $Zn_{0.2}Ni_{0.8}O$@CF electrode, thus providing superior rate capability and lower energy consumption [78]. The Trasatti analysis method was used to further analyze electrochemical kinetics of the $Zn_{0.2}Ni_{0.8}O$@CF sample. This approach differentiated the surface-controlled capacity of $Zn_{0.2}Ni_{0.8}O$@CF electrode into "inner" and "outer" surface control (more details in Supporting Information) [63]. The "inner" surface referred to the regions of difficult accessibility, while the "outer" surface mainly came from the surface exposed directly to ions and was unaffected by sweep rates. The calculation was based on Eqs. (3) and (4):

$$q^{*} = q_{s,out} + A_1 \nu^{-1/2} (\nu \to \infty) \quad (3)$$

$$q^{*-1} = q_{s}^{-1} + A_2 \nu^{1/2} (\nu \to 0) \quad (4)$$

where q^* was the voltammetric charge, $q_{s,out}$ was the "outer" capacity, and q_s was the surface-controlled capacity. $q_{s,out}$ was calculated to be 154.1 mF cm^{-2}, constituting 43.2% of q_s, which was a relatively very high value [79].

The specific capacitance was 82.13% of the total specific capacitance at the scan rate of 1 mV s^{-1}, indicating a prominent electrochemical utilization ratio for $Zn_{0.2}Ni_{0.8}O$@CF. This indicated that $Zn_{0.2}Ni_{0.8}O$@CF electrode offered rapid, capacitor-like ion removal and charge transfer (Fig. 4b), which was beneficial to enhance charge-storage kinetics.

To gain further insight into the mass transport of Na^+ during the adsorption process, we detected the relationship between mass and charge capacity change of electrode materials in the electrochemical process by EQCM-D. As shown in Fig. 4c, significant changes in the frequency factor of the $Zn_{0.2}Ni_{0.8}O$@CF electrode can be observed during the CV process. Under the condition of various scan rates, the frequency responses basically returned to their initial values and showed good periodic changes, indicating that on the experimental timescale, the mass changes were recoverable and excellent stability of the $Zn_{0.2}Ni_{0.8}O$@CF electrode [80]. EQCM-D results of the 3rd cycle showed that the frequency ($\Delta f_5/5$) decreased at varying scan rates (Fig. S9a), indicating that the mass of the $Zn_{0.2}Ni_{0.8}O$@CF electrode increased qualitatively as a result of the Na^+ adsorption process; additionally, $\Delta f_5/5$ returned to approximately 0 Hz, demonstrating the Na^+ desorption process caused the decrease in the electrode mass. It was noteworthy that dissipation factor (D) corresponding change showed a similar trend, decreasing first and then returning to the initial value (Fig. S9b), indicating the absorption of ions on the $Zn_{0.2}Ni_{0.8}O$@CF electrode was reversible, thus confirming the stability of the $Zn_{0.2}Ni_{0.8}O$@CF electrode. The decrease in D when the electrode lost energy quickly implied that adsorbate on the $Zn_{0.2}Ni_{0.8}O$@CF surface was rigid and compact [81]. In this case, CV curve of the 3th cycle and the simultaneous EQCM-D response were shown in Fig. 4d, and the corresponding $\Delta m - \Delta Q$ plot was calculated and shown in Fig. 4e. We found that the electrode mass increases uniformly when the material charge increases; while when the current was reversed ($\Delta Q \approx 0$), the Δm trend changes and the electrode mass starts to decrease, indicating that

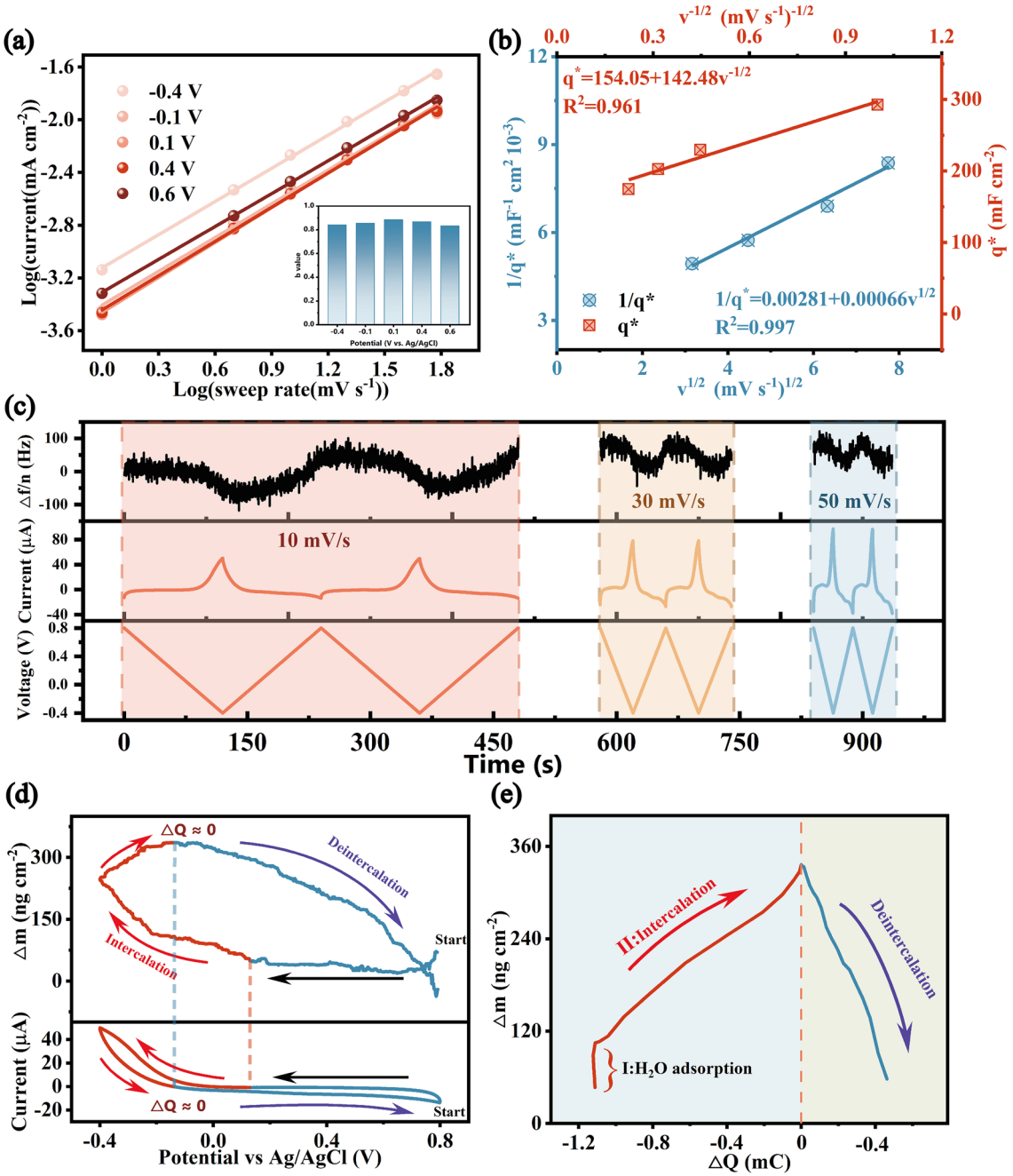

Fig. 4 **a** Calculation of b-values of $Zn_{0.2}Ni_{0.8}O$ based on CV curves. **b** The relationship between $1/q^*$ and $v^{1/2}$ and between q^* and $v^{-1/2}$. **c** △f/5 responses of $Zn_{0.2}Ni_{0.8}O$ from EQCM-D during CV at different scan rates. The simultaneous **d** mass change and current response and **e** change in electrode mass versus charge passed during $Zn_{0.2}Ni_{0.8}O$ electrode adsorption/desorption processes at 10 mV s^{-1} between −0.4 ~ 0.8 V. Blue region highlights the process of adsorption and yellow highlights the process of desorption

the material has excellent pseudocapacitive properties and the de-/intercalation process has a high sensitivity to the current response due to the rapid transfer process. The mass change of electrode closely followed the theoretical mass change in stages II and III, indicating that all of the charges were applied for sodium-ion intercalation and no other side reactions occurred. The Sauerbrey's equation was applied to analyze the EQCM-D results to quantify the mass changes of the $Zn_{0.2}Ni_{0.8}O$@CF [82]. The Red I region of the △m increased without the change in △Q may be the

 https://doi.org/10.1007/s40820-024-01371-y

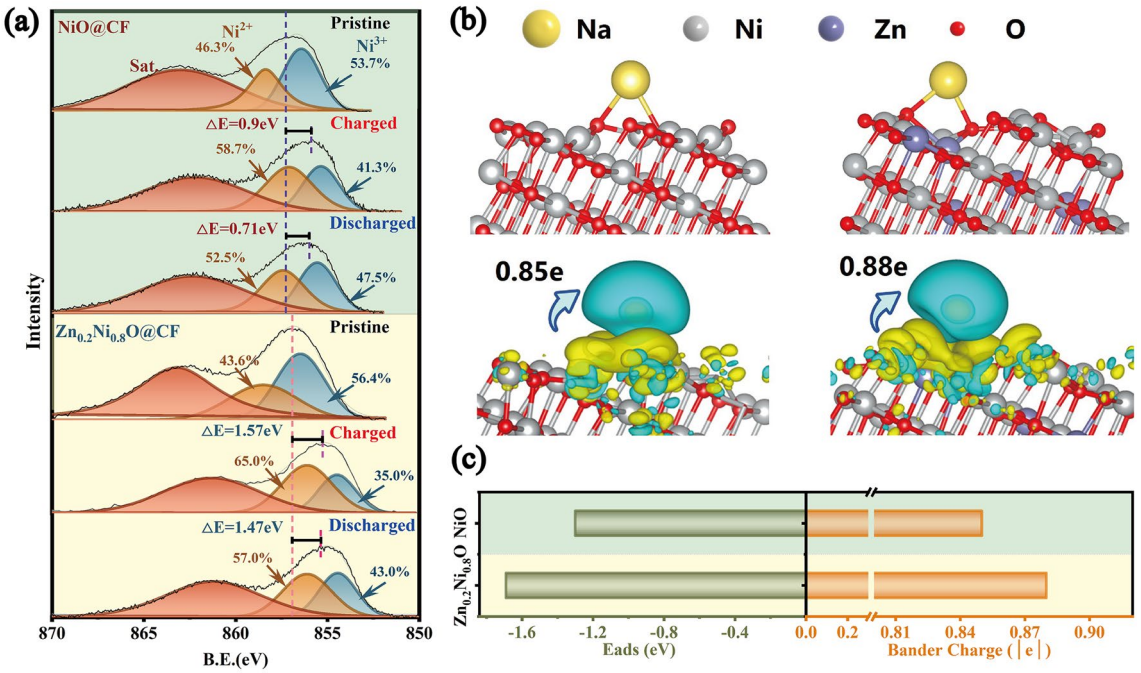

Fig. 5 **a** Ex situ XPS spectra/data of Ni $2p_{3/2}$ of NiO and $Zn_{0.2}Ni_{0.8}O$ electrodes in original states and in completely adsorption/desorption states after the third desalination cycle at ± 1.4 V at 1000 mA cm^{-2}. **b** Side view of relaxed adsorption configurations for corresponding E_{ads} for Na^+ on NiO and $Zn_{0.2}Ni_{0.8}O$ with (225) surfaces, along with the Bader charge and difference charge density analysis. **c** E_{ads} and Bader charge for single Na^+ analysis of the electrodes

adsorption process of water molecules. The MPE value in the adsorption region (Red II) was 20.68 g mol^{-1}, which was marginally lower than 23 g mol^{-1}, demonstrating that Na^+ adsorption was the main process in this region after partial desolvation of sodium hydrate. However, in the desorption region (Blue), the MPE value was 45.16 g mol^{-1}, indicating that this process was co-deintercalation of a water molecule and a Na^+ ion. The EQCM-D data revealed the excellent pseudocapacitive properties of the material, the mechanism of the ion storage process (intercalation of one sodium ion and co-deintercalation of one sodium ion with one water molecule) and a high degree of sodium-ion adsorption reversibility within the electrochemical processes of sodium storage of $Zn_{0.2}Ni_{0.8}O$@CF.

It was widely recognized that the electrochemical performance was closely linked to the surface electroactive sites. To comparatively investigate surface chemical structure of $Zn_{0.2}Ni_{0.8}O$@CF and NiO@CF electrodes, the ex-situ XPS was then used. Figure S10 shows the Zn 2*p* spectra of $Zn_{0.2}Ni_{0.8}O$@CF electrode in pristine states and in full adsorption/desorption states.

It was observed that the Zn valence remained unchanged within the electrochemical processes, which once again proved that Zn was a redox-inert specie in the $Zn_{0.2}Ni_{0.8}O$@CF. However, in this case, an interesting finding has been found, that was, the electrochemical performance of $Zn_{0.2}Ni_{0.8}O$@CF electrode, which contained 82% redox-active Ni species and 18% Zn redox-inert species, was even slightly better than that of the NiO@CF electrode, which was composed of 100% redox-active Ni species. Thus, an attempt has been made to elucidate the hidden reasons for the interesting phenomenon from the perspective of activity–structure relationship. Figure 5a displayed ex situ XPS spectra of Ni $2p_{3/2}$ of NiO@CF and $Zn_{0.2}Ni_{0.8}O$@CF electrodes in original states and in fully adsorption/desorption states at the third desalination cycle of 1000 mA cm^{-2}. Upon careful comparison of the changes in peak binding energy between original and completely adsorbed/desorbed states (Table S4), it can be seen that the $Zn_{0.2}Ni_{0.8}O$@CF electrode exhibited much larger changes of Ni $2p_{3/2}$ (1.47/1.57 eV) than the NiO@CF electrode (0.9/0.71 eV); furthermore, the relative ratio changes of Ni with 3 + /2 + valences of the $Zn_{0.2}Ni_{0.8}O$@CF electrode in fully adsorbed and

desorbed states ($Ni^{3+} \rightarrow Ni^{2+}$: △Ni 8%) are higher than that ($Ni^{3+} \rightarrow Ni^{2+}$: △Ni 6.2%) of the NiO@CF. The change in the ratios of Ni valences indicated the presence of different electroactive sites on surface during electrochemical processes. The higher conversion between Ni^{3+} and Ni^{2+} species during the adsorption/desorption process suggested more oxidations and reductions of Ni active species (Ni^{3+}/Ni^{2+}) with larger charge transfer ability [46], proving the superior electroactive sites on surface and promoted reaction kinetics of the $Zn_{0.2}Ni_{0.8}O$@CF due to Zn-doping.

To gain better insights of the improved performance of $Zn_{0.2}Ni_{0.8}O$@CF electrode due to Zn-doping, we employed DFT to analyze Na^+ adsorbed thermodynamics, including Na^+ adsorbed energy and difference charge density in the $Zn_{0.2}Ni_{0.8}O$@CF and NiO@CF electrodes. It was reported that the adsorption capability and charge transfer ability of surface-active metals of electrodes were closely linked to electrochemical activity [83, 84]. Figures 5b, c and S11 show Bader charge analysis, difference charge density, the adsorption energy of Na^+ (E_{ads}) and the optimized structural models of the NiO@CF and $Zn_{0.2}Ni_{0.8}O$@CF with (225) surfaces. In Fig. 5c, the $Zn_{0.2}Ni_{0.8}O$@CF showed much more negative average E_{ads} of Na^+ (− 1.96 eV) to those of the NiO (− 1.30 eV), proving the superior thermodynamic adsorption of Na^+. In all instances, there was a net increase in electrons on the O atoms, while there was a net decrease in electrons on Na^+, indicating a substantial charge transfer from Na^+ to surface [85]. The analysis of Bader charge (Fig. 5c) additionally confirmed this result, showing that 0.88e were transferred from Na^+ to the surface of $Zn_{0.2}Ni_{0.8}O$@CF, which is higher than the amount transferred to the NiO@CF electrode (0.85e). Since the neutral and isolated systems were utilized in the system, electrons could not be transferred to external circuit. Consequently, transfer of a greater number of electrons from Na^+ to the surface implied improved capability of electronic transfer of the surface to the external circuit when the constant voltage was applied. So, in this case, the superior adsorption thermodynamic of Na^+ and charge transfer capability could promote the electrochemical reactions and consequently improve the reaction activity. The analysis of DFT further illustrated that $Zn_{0.2}Ni_{0.8}O$@CF electrode activity can be adequately promoted by the Zn-doping.

4 Conclusion

In this study, by simply adjusting the pH of the pre-mixture conditions, we constrained the rate of OH^- generation and thus the number of lamellar nuclei formation, then prepared the $Zn_{0.2}Ni_{0.8}O$@CF electrode with a high-density hierarchical structure with three-dimensional open pores, which has more ion accessible surface area and high-speed ion conductive network. The $Zn_{0.2}Ni_{0.8}O$@CF electrode exhibited high desalination capacity (128.9 mg_{NaCl} g^{-1}), fast rate capability (1.21 mg_{NaCl} g^{-1} min^{-1}), low energy consumption (0.164 kW h $kg_{NaCl}{}^{-1}$), and high cyclability, outperforming the desalination performance of cutting-edge CDI electrodes. In addition to the kinetic convenience provided by the surface nanostructures, the excellent electrochemical performance was also improved from kinetic and thermodynamic perspectives by appropriate amounts of Zn-doping. Ex situ XPS and DFT analysis demonstrated that Zn-doping can be an active promoter to enhance the surface electroactive sites, real activity of redox-active Ni species, thus reduce the sodium adsorption energy of the $Zn_{0.2}Ni_{0.8}O$@CF electrode. The EQCM-D provided unequivocal evidence that the $Zn_{0.2}Ni_{0.8}O$@CF had high-speed charge-mass correspondence and Na^+ was inserted into the material alone, and one Na^+ ion was co-deintercalation with one water molecule. In this study, a new horizon was opened regarding the regulation of electrochemically favorable micromorphology, and the redox-inert Zn-doping was pivotal to promoting actual activity of reaction sites.

Acknowledgements This research is supported by The National Natural Science Foundation of China (22276137, 52170087) and the Fundamental Research Funds for the Central Universities (XJEDU2023Z009). We are also thankful to the anonymous reviewers for their valuable comments to improve this manuscript.

Declarations

Conflict of interest The author declares no interest conflict. They have no known competing financial interests or personal relationships that could have appeared to influence the work reported in this paper.

Supplementary Information The online version contains supplementary material available at https://doi.org/10.1007/s40820-024-01371-y.

References

1. M. Metzger, M.M. Besli, S. Kuppan, S. Hellstrom, S. Kim et al., Techno-economic analysis of capacitive and intercalative water deionization. Energy Environ. Sci. **13**, 1544–1560 (2020). https://doi.org/10.1039/D0EE00725K
2. P. Srimuk, X. Su, J. Yoon, D. Aurbach, V. Presser, Charge-transfer materials for electrochemical water desalination, ion separation and the recovery of elements. Nat. Rev. Mater. **5**, 517–538 (2020). https://doi.org/10.1038/s41578-020-0193-1
3. C. Chen, C.-S. Lee, Y. Tang, Fundamental understanding and optimization strategies for dual-ion batteries: a review. Nano-Micro Lett. **15**, 121 (2023). https://doi.org/10.1007/s40820-023-01086-6
4. X. Zhao, H. Wei, H. Zhao, Y. Wang, N. Tang, Electrode materials for capacitive deionization: a review. J. Electroanal. Chem. **873**, 114416 (2020). https://doi.org/10.1016/j.jelechem.2020.114416
5. W. Tang, D. He, C. Zhang, P. Kovalsky, T.D. Waite, Comparison of Faradaic reactions in capacitive deionization (CDI) and membrane capacitive deionization (MCDI) water treatment processes. Water Res. **120**, 229–237 (2017). https://doi.org/10.1016/j.watres.2017.05.009
6. J. Lee, S. Kim, C. Kim, J. Yoon, Hybrid capacitive deionization to enhance the desalination performance of capacitive techniques. Energy Environ. Sci. **7**, 3683–3689 (2014). https://doi.org/10.1039/C4EE02378A
7. S. Porada, R. Zhao, A. van der Wal, V. Presser, P.M. Biesheuvel, Review on the science and technology of water desalination by capacitive deionization. Prog. Mater. Sci. **58**, 1388–1442 (2013). https://doi.org/10.1016/j.pmatsci.2013.03.005
8. Y. Jiang, L. Chai, D. Zhang, F. Ouyang, X. Zhou et al., Facet-controlled $LiMn_2O_4$/C as deionization electrode with enhanced stability and high desalination performance. Nano-Micro Lett. **14**, 176 (2022). https://doi.org/10.1007/s40820-022-00897-3
9. Z. Liu, H. Li, Exploration of the exceptional capacitive deionization performance of $CoMn_2O_4$ microspheres electrode. Energy Environ. Mater. **6**, 12255 (2023). https://doi.org/10.1002/eem2.12255
10. S. Wang, G. Wang, T. Wu, C. Li, Y. Wang et al., Membrane-free hybrid capacitive deionization system based on redox reaction for high-efficiency NaCl removal. Environ. Sci. Technol. **53**, 6292–6301 (2019). https://doi.org/10.1021/acs.est.9b00662
11. J. Ma, Y. Xiong, X. Dai, F. Yu, Zinc spinel ferrite nanoparticles as a pseudocapacitive electrode with ultrahigh desalination capacity and long-term stability. Environ. Sci. Technol. Lett. **7**, 118–125 (2020). https://doi.org/10.1021/acs.estlett.0c00027
12. M. Liang, X. Bai, F. Yu, J. Ma, A confinement strategy to in situ prepare a peanut-like N-doped, C-wrapped TiO_2 electrode with an enhanced desalination capacity and rate for capacitive deionization. Nano Res. **14**, 684–691 (2021). https://doi.org/10.1007/s12274-020-3097-x
13. F. Yu, H. Yin, X. Bai, J. Pan, X. Zhang et al., Cu@Cu_2O/carbon for efficient desalination in capacitive deionization. Chin. Chem. Lett. **34**, 108362 (2023). https://doi.org/10.1016/j.cclet.2023.108362
14. X. Zhang, E.A. Toledo-Carrillo, D. Yu, J. Dutta, Effect of surface charge on the fabrication of hierarchical Mn-based Prussian blue analogue for capacitive desalination. ACS Appl. Mater. Interfaces **14**, 40371–40381 (2022). https://doi.org/10.1021/acsami.2c08192
15. W. Shi, X. Liu, T. Deng, S. Huang, M. Ding et al., Enabling superior sodium capture for efficient water desalination by a tubular polyaniline decorated with Prussian blue nanocrystals. Adv. Mater. **32**, 1907404 (2020). https://doi.org/10.1002/adma.201907404
16. J. Guo, Y. Wang, Y. Cai, H. Zhang, Y. Li et al., Ni-doping Cu-Prussian blue analogue/carbon nanotubes composite (Ni–CuPBA/CNTs) with 3D electronic channel-rich network structure for capacitive deionization. Desalination **528**, 115622 (2022). https://doi.org/10.1016/j.desal.2022.115622
17. J. Cao, Y. Wang, L. Wang, F. Yu, J. Ma, $Na_3V_2(PO_4)_3$@C as faradaic electrodes in capacitive deionization for high-performance desalination. Nano Lett. **19**, 823–828 (2019). https://doi.org/10.1021/acs.nanolett.8b04006
18. S. Xing, Y. Cheng, F. Yu, J. Ma, $Na_3(VO)_2(PO_4)_2F$ nanocuboids/graphene hybrid materials as faradic electrode for extra-high desalination capacity. J. Colloid Interface Sci. **598**, 511–518 (2021). https://doi.org/10.1016/j.jcis.2021.04.051
19. J. Lei, Y. Xiong, F. Yu, J. Ma, Flexible self-supporting CoFe-LDH/MXene film as a chloride ions storage electrode in capacitive deionization. Chem. Eng. J. **437**, 135381 (2022). https://doi.org/10.1016/j.cej.2022.135381
20. M. Liang, L. Wang, V. Presser, X. Dai, F. Yu et al., Combining battery-type and pseudocapacitive charge storage in Ag/$Ti_3C_2t_x$ MXene electrode for capturing chloride ions with high capacitance and fast ion transport. Adv. Sci. **7**, e2000621 (2020). https://doi.org/10.1002/advs.202000621
21. X. Shen, Y. Xiong, R. Hai, F. Yu, J. Ma, All-MXene-based integrated membrane electrode constructed using $Ti_3C_2T_x$ as an intercalating agent for high-performance desalination. Environ. Sci. Technol. **54**, 4554–4563 (2020). https://doi.org/10.1021/acs.est.9b05759
22. J. Zhang, J. Wang, F. Zhu, P. Mao, Z. Wu et al., Dispersing bentonite by electron beam irradiation and its adsorption performance of Cr(VI) in the aqueous solution. Water Air Soil Pollut. **233**, 503 (2022). https://doi.org/10.1007/s11270-022-05980-4

23. Y. Xiong, F. Yu, S. Arnold, L. Wang, V. Presser et al., Three-dimensional cobalt hydroxide hollow cube/vertical nanosheets with high desalination capacity and long-term performance stability in capacitive deionization. Research **2021**, 9754145 (2021). https://doi.org/10.34133/2021/9754145
24. F. Yu, L. Wang, Y. Wang, X. Shen, Y. Cheng et al., Faradaic reactions in capacitive deionization for desalination and ion separation. J. Mater. Chem. A **7**, 15999–16027 (2019). https://doi.org/10.1039/C9TA01264H
25. X. He, Fundamental perspectives on the electrochemical water applications of metal–organic frameworks. Nano-Micro Lett. **15**, 148 (2023). https://doi.org/10.1007/s40820-023-01124-3
26. Y. Li, J. Jiao, Q. Wu, Q. Song, W. Xie et al., Environmental applications of graphene oxide composite membranes. Chin. Chem. Lett. **33**, 5001–5012 (2022). https://doi.org/10.1016/j.cclet.2022.01.034
27. S. Chen, Q. Wen, Y. Zhu, Y. Ji, Y. Pu et al., Boron-promoted reductive deoxygenation coupling reaction of sulfonyl chlorides for the C(sp3)-S bond construction. Chin. Chem. Lett. **33**, 5101–5105 (2022). https://doi.org/10.1016/j.cclet.2022.04.022
28. X. Cai, J. Du, G. Zhong, Y. Zhang, L. Mao et al., Constructing a $CeO_2/Zn_xCd_{1-x}In_2S_4$ S-scheme hollow heterostructure for efficient photocatalytic H_2 evolution. Acta Phys. Chim. Sin. (2023). https://doi.org/10.3866/pku.whxb202302017
29. Y. Chen, C. Chen, X. Cao, Z. Wang, N. Zhang et al., Recent advances in defect and interface engineering for electroreduction of CO_2 and N_2. Acta Phys. Chim. Sin. (2023). https://doi.org/10.3866/pku.whxb202212053
30. W. Jiang, H. Jiang, W. Liu, X. Guan, Y. Li et al., Pickering emulsion templated proteinaceous microsphere with bio-stimuli responsiveness. Acta Phys. Chim. Sin. (2023). https://doi.org/10.3866/pku.whxb202301041
31. X. Wang, Y. Cheng, G. Xue, Z. Zhou, M. Zhao et al., Giant enhancement of optical second harmonic generation in hollow-core fiber integrated with GaSe nanoflakes. Acta Phys. Chim. Sin. (2023). https://doi.org/10.3866/pku.whxb202212028
32. Y. Xiong, F. Yu, J. Ma, Research progress in chlorine ion removal electrodes for desalination by capacitive deionization. Acta Phys. Chim. Sin. **38**, 2006037 (2020). https://doi.org/10.3866/pku.whxb202006037
33. J. Mou, L. Chen, J. Fan, L. Zeng, X. Jiang et al., Construction of a highly active Rh/CeO_2-ZrO_2-Al_2O_3 catalyst based on Rh micro-chemical state regulation and its three-way catalytic activity. Acta Phys. Chim. Sin. **39**, 2302041 (2023). https://doi.org/10.3866/pku.whxb202302041
34. N. Yabuuchi, K. Kubota, M. Dahbi, S. Komaba, Research development on sodium-ion batteries. Chem. Rev. **114**, 11636–11682 (2014). https://doi.org/10.1021/cr500192f
35. S.P. Ong, V.L. Chevrier, G. Hautier, A. Jain, C. Moore et al., Voltage, stability and diffusion barrier differences between sodium-ion and lithium-ion intercalation materials. Energy Environ. Sci. **4**, 3680–3688 (2011). https://doi.org/10.1039/C1EE01782A
36. A. Ali, M. Ammar, A. Mukhtar, T. Ahmed, M. Ali et al., 3D NiO nanowires@NiO nanosheets core-shell structures grown on nickel foam for high performance supercapacitor electrode. J. Electroanal. Chem. **857**, 113710 (2020). https://doi.org/10.1016/j.jelechem.2019.113710
37. B. Gnana Sundara Raj et al., Pseudocapacitive properties of nickel oxide nanoparticles synthesized via ultrasonication approach. Ionics **26**, 953–960 (2020). https://doi.org/10.1007/s11581-019-03236-6
38. C. Yuan, X. Zhang, L. Su, B. Gao, L. Shen, Facile synthesis and self-assembly of hierarchical porous NiO nano/micro spherical superstructures for high performance supercapacitors. J. Mater. Chem. **19**, 5772–5777 (2009). https://doi.org/10.1039/B902221J
39. L. Fang, C. Wang, L. Huangfu, N. Bahlawane, H. Tian et al., Enabling full conversion reaction with high reversibility to approach theoretical capacity for sodium storage. Adv. Funct. Mater. **29**, 1906680 (2019). https://doi.org/10.1002/adfm.201906680
40. L. Fang, Z. Lan, W. Guan, P. Zhou, N. Bahlawane et al., Hetero-interface constructs ion reservoir to enhance conversion reaction kinetics for sodium/lithium storage. Energy Storage Mater. **18**, 107–113 (2019). https://doi.org/10.1016/j.ensm.2018.10.002
41. X. Xiong, C. Yang, G. Wang, Y. Lin, X. Ou et al., SnS nanoparticles electrostatically anchored on three-dimensional N-doped graphene as an active and durable anode for sodium-ion batteries. Energy Environ. Sci. **10**, 1757–1763 (2017). https://doi.org/10.1039/C7EE01628J
42. M. Okubo, E. Hosono, J. Kim, M. Enomoto, N. Kojima et al., Nanosize effect on high-rate Li-ion intercalation in $LiCoO_2$ electrode. J. Am. Chem. Soc. **129**, 7444–7452 (2007). https://doi.org/10.1021/ja0681927
43. P. Simon, Y. Gogotsi, B. Dunn, Where do batteries end and supercapacitors begin? Science **343**, 1210–1211 (2014). https://doi.org/10.1126/science.1249625
44. S. Wang, Y. Zou, F. Xu, C. Xiang, H. Peng et al., Morphological control and electrochemical performance of $NiCo_2O_4$@NiCo layered double hydroxide as an electrode for supercapacitors. J. Energy Storage **41**, 102862 (2021). https://doi.org/10.1016/j.est.2021.102862
45. J.A. Dawson, M.S. Islam, A nanoscale design approach for enhancing the Li-ion conductivity of the $Li_{10}GeP_2S_{12}$ solid electrolyte. ACS Mater. Lett. **4**, 424–431 (2022). https://doi.org/10.1021/acsmaterialslett.1c00766
46. Z. Jia, R. Ding, W. Yu, Y. Li, A. Wang et al., Unraveling the charge storage and activity-enhancing mechanisms of Zn-doping perovskite fluorides and engineering the electrodes and electrolytes for wide-temperature aqueous supercabatteries. Adv. Funct. Mater. **32**, 2107674 (2022). https://doi.org/10.1002/adfm.202107674
47. S. Cao, Y. Li, Y. Tang, Y. Sun, W. Li et al., Space-confined metal ion strategy for carbon materials derived from cobalt benzimidazole frameworks with high desalination performance in simulated seawater. Adv. Mater. **35**, e2301011 (2023). https://doi.org/10.1002/adma.202301011

 https://doi.org/10.1007/s40820-024-01371-y

48. H. Zhou, G. Zhu, S. Dong, P. Liu, Y. Lu et al., Ethanol-induced Ni^{2+}-intercalated cobalt organic frameworks on vanadium pentoxide for synergistically enhancing the performance of 3D-printed micro-supercapacitors. Adv. Mater. **35**, e2211523 (2023). https://doi.org/10.1002/adma.202211523
49. X.-T. Wang, T. Ouyang, L. Wang, J.-H. Zhong, Z.-Q. Liu, Surface reorganization on electrochemically-induced Zn–Ni-co spinel oxides for enhanced oxygen electrocatalysis. Angew. Chem. Int. Ed. **59**, 6492–6499 (2020). https://doi.org/10.1002/anie.202000690
50. X. Liu, Z. Chang, L. Luo, T. Xu, X. Lei et al., Hierarchical $Zn_xCo_{3-x}O_4$ nanoarrays with high activity for electrocatalytic oxygen evolution. Chem. Mater. **26**, 1889–1895 (2014). https://doi.org/10.1021/cm4040903
51. J. Li, Z. Liu, Q. Zhang, Y. Cheng, B. Zhao et al., Anion and cation substitution in transition-metal oxides nanosheets for high-performance hybrid supercapacitors. Nano Energy **57**, 22–33 (2019). https://doi.org/10.1016/j.nanoen.2018.12.011
52. Z. Li, M. Shao, L. Zhou, R. Zhang, C. Zhang et al., A flexible all-solid-state micro-supercapacitor based on hierarchical CuO@layered double hydroxide core–shell nanoarrays. Nano Energy **20**, 294–304 (2016). https://doi.org/10.1016/j.nanoen.2015.12.030
53. S.-I. Kim, J.-S. Lee, H.-J. Ahn, H.-K. Song, J.-H. Jang, Facile route to an efficient NiO supercapacitor with a three-dimensional nanonetwork morphology. ACS Appl. Mater. Interfaces **5**, 1596–1603 (2013). https://doi.org/10.1021/am3021894
54. X. Lou, C. Yuan, E. Rhoades, Q. Zhang, L. Archer, Encapsulation and Ostwald ripening of Au and Au–Cl complex nanostructures in silica shells. Adv. Funct. Mater. **16**, 1679–1684 (2006). https://doi.org/10.1002/adfm.200500909
55. C.-Y. Cao, W. Guo, Z.-M. Cui, W.-G. Song, W. Cai, Microwave-assisted gas/liquid interfacial synthesis of flowerlike NiO hollow nanosphere precursors and their application as supercapacitor electrodes. J. Mater. Chem. **21**, 3204–3209 (2011). https://doi.org/10.1039/C0JM03749D
56. T. Liu, J. Serrano, J. Elliott, X. Yang, W. Cathcart et al., Exceptional capacitive deionization rate and capacity by block copolymer-based porous carbon fibers. Sci. Adv. **6**, 0906 (2020). https://doi.org/10.1126/sciadv.aaz0906
57. X. Gong, S. Zhang, W. Luo, N. Guo, L. Wang et al., Enabling a large accessible surface area of a pore-designed hydrophilic carbon nanofiber fabric for ultrahigh capacitive deionization. ACS Appl. Mater. Interfaces **12**, 49586–49595 (2020). https://doi.org/10.1021/acsami.0c13503
58. H. Chen, L. Hu, M. Chen, Y. Yan, L. Wu, Nickel–cobalt layered double hydroxide nanosheets for high-performance supercapacitor electrode materials. Adv. Funct. Mater. **24**, 934–942 (2014). https://doi.org/10.1002/adfm.201301747
59. Q. Pan, F. Zheng, D. Deng, B. Chen, Y. Wang, Interlayer spacing regulation of NiCo-LDH nanosheets with ultrahigh specific capacity for battery-type supercapacitors. ACS Appl. Mater. Interfaces **13**, 56692–56703 (2021). https://doi.org/10.1021/acsami.1c19320
60. D. Li, S. Wang, G. Wang, C. Li, X. Che et al., Facile fabrication of NiCoAl-layered metal oxide/graphene nanosheets for efficient capacitive deionization defluorination. ACS Appl. Mater. Interfaces **11**, 31200–31209 (2019). https://doi.org/10.1021/acsami.9b10307
61. B. Peng, Y. Chen, F. Wang, Z. Sun, L. Zhao et al., Unusual site-selective doping in layered cathode strengthens electrostatic cohesion of alkali-metal layer for practicable sodium-ion full cell. Adv. Mater. **34**, e2103210 (2022). https://doi.org/10.1002/adma.202103210
62. Q. Yin, D. Rao, G. Zhang, Y. Zhao, J. Han et al., CoFe–Cl layered double hydroxide: a new cathode material for high-performance chloride ion batteries. Adv. Funct. Mater. **29**, 1900983 (2019). https://doi.org/10.1002/adfm.201900983
63. S. Fleischmann, J.B. Mitchell, R. Wang, C. Zhan, D.-E. Jiang et al., Pseudocapacitance: from fundamental understanding to high power energy storage materials. Chem. Rev. **120**, 6738–6782 (2020). https://doi.org/10.1021/acs.chemrev.0c00170
64. J. Ji, L.L. Zhang, H. Ji, Y. Li, X. Zhao et al., Nanoporous $Ni(OH)_2$ thin film on 3D Ultrathin-graphite foam for asymmetric supercapacitor. ACS Nano **7**, 6237–6243 (2013). https://doi.org/10.1021/nn4021955
65. X. Lu, D. Zheng, T. Zhai, Z. Liu, Y. Huang et al., Facile synthesis of large-area manganese oxide nanorod arrays as a high-performance electrochemical supercapacitor. Energy Environ. Sci. **4**, 2915–2921 (2011). https://doi.org/10.1039/C1EE01338F
66. J. Guo, X. Xu, J.P. Hill, L. Wang, J. Dang et al., Graphene–carbon 2D heterostructures with hierarchically-porous P, N-doped layered architecture for capacitive deionization. Chem. Sci. **12**, 10334–10340 (2021). https://doi.org/10.1039/D1SC00915J
67. B. Zhao, R. Wang, Y. Li, Y. Ren, X. Li et al., Dependence of electromagnetic interference shielding ability of conductive polymer composite foams with hydrophobic properties on cellular structure. J. Mater. Chem. C **8**, 7401–7410 (2020). https://doi.org/10.1039/D0TC00987C
68. M.E. Suss, S. Porada, X. Sun, P.M. Biesheuvel, J. Yoon et al., Water desalination *via* capacitive deionization: what is it and what can we expect from it? Energy Environ. Sci. **8**, 2296–2319 (2015). https://doi.org/10.1039/C5EE00519A
69. C. Zhang, D. Wang, Z. Wang, G. Zhang, Z. Liu et al., Boosting capacitive deionization performance of commercial carbon fibers cloth via structural regulation based on catalytic-etching effect. Energy Environ. Mater. **6**, 12276 (2023). https://doi.org/10.1002/eem2.12276
70. W. Lei, J. Liang, P. Tan, S. Yang, L. Fan et al., Preparation of edible starch nanomaterials for the separation of polyphenols from fruit pomace extract and determination of their adsorption properties. Int. J. Biol. Macromol. **222**, 2054–2064 (2022). https://doi.org/10.1016/j.ijbiomac.2022.10.004
71. R. Liu, Y. Wang, Y. Wu, X. Ye, W. Cai, Controllable synthesis of nickel–cobalt-doped Prussian blue analogs for capacitive desalination. Electrochim. Acta **442**, 141815 (2023). https://doi.org/10.1016/j.electacta.2023.141815
72. N. Liu, L. Yu, B. Liu, F. Yu, L. Li et al., Ti_3C_2-MXene partially derived hierarchical 1D/2D TiO_2/Ti_3C_2 heterostructure electrode for high-performance capacitive deionization. Adv.

Sci. **10**, 2204041 (2023). https://doi.org/10.1002/advs.202204041

73. H.-Y. Huang, Y.-H. Tu, Y.-H. Yang, Y.-T. Lu, C.-C. Hu, Dopant-designed conducting polymers for constructing a high-performance, electrochemical deionization system achieving low energy consumption and long cycle life. Chem. Eng. J. **457**, 141373 (2023). https://doi.org/10.1016/j.cej.2023.141373
74. J. Liang, J. Yu, W. Xing, W. Tang, N. Tang et al., 3D interconnected network architectures assembled from $W_{18}O_{49}$ and Ti_3C_2 MXene with excellent electrochemical properties and CDI performance. Chem. Eng. J. **435**, 134922 (2022). https://doi.org/10.1016/j.cej.2022.134922
75. Z. Bo, Z. Huang, C. Xu, Y. Chen, E. Wu et al., Anion-kinetics-selective graphene anode and cation-energy-selective MXene cathode for high-performance capacitive deionization. Energy Storage Mater. **50**, 395–406 (2022). https://doi.org/10.1016/j.ensm.2022.05.042
76. Q. Li, X. Xu, J. Guo, J.P. Hill, H. Xu et al., Two-dimensional MXene-polymer heterostructure with ordered In-plane mesochannels for high-performance capacitive deionization. Angew. Chem. Int. Ed. **60**, 26528–26534 (2021). https://doi.org/10.1002/anie.202111823
77. A. Amiri, Y. Chen, C. Bee Teng, M. Naraghi, Porous nitrogen-doped MXene-based electrodes for capacitive deionization. Energy Storage Mater. **25**, 731–739 (2020). https://doi.org/10.1016/j.ensm.2019.09.013
78. H.-S. Kim, J.B. Cook, H. Lin, J.S. Ko, S.H. Tolbert et al., Oxygen vacancies enhance pseudocapacitive charge storage properties of MoO_{3-x}. Nat. Mater. **16**, 454–460 (2017). https://doi.org/10.1038/nmat4810
79. R. Niu, H. Li, Y. Ma, L. He, J. Li An, insight into the improved capacitive deionization performance of activated carbon treated by sulfuric acid. Electrochim. Acta **176**, 755–762 (2015). https://doi.org/10.1016/j.electacta.2015.07.012
80. S. Wang, F. Li, A.D. Easley, J.L. Lutkenhaus, Real-time insight into the doping mechanism of redox-active organic radical polymers. Nat. Mater. **18**, 69–75 (2019). https://doi.org/10.1038/s41563-018-0215-1
81. N. Shpigel, M.D. Levi, S. Sigalov, O. Girshevitz, D. Aurbach et al., In situ hydrodynamic spectroscopy for structure characterization of porous energy storageelectrodes. Nat. Mater. **15**, 570–575 (2016). https://doi.org/10.1038/nmat4577
82. P. Roach, D. Farrar, C.C. Perry, Interpretation of protein adsorption: surface-induced conformational changes. J. Am. Chem. Soc. **127**, 8168–8173 (2005). https://doi.org/10.1021/ja042898o
83. X. Sun, J. Sun, C. Wu, L. Guo, L. Hou et al., Unveiling composition/crystal structure-dependent electrochemical behaviors via experiments and first-principles calculations: rock-salt $NiCoO_2$ vs. spinel $Ni_{1.5}Co_{1.5}O_4$. Mater. Today Energy **19**, 100592 (2021). https://doi.org/10.1016/j.mtener.2020.100592
84. J. Yang, C. Yu, X. Fan, S. Liang, S. Li et al., Electroactive edge site-enriched nickel–cobalt sulfide into graphene frameworks for high-performance asymmetric supercapacitors. Energy Environ. Sci. **9**, 1299–1307 (2016). https://doi.org/10.1039/C5EE03633J
85. Z. Wang, Z. Zhao, Y. Zhang, X. Yang, X. Sun et al., Spatially self-confined formation of ultrafine $NiCoO_2$ Nanoparticles@Ultralong amorphous N-doped carbon nanofibers as an anode towards efficient capacitive Li^+ storage. Chemistry **25**, 863–873 (2019). https://doi.org/10.1002/chem.201804823

 https://doi.org/10.1007/s40820-024-01371-y